Polyoxometalate-based Complex@Graphene Composite Electrodes for Efficient Nitrate Reduction to Ammonia

Nan Zhao[a], Xinming Wang*[a], Shuang Rong[b], Qiushuang Jiang[a], Haoyun Li[a], Haijun Pang*[a], Huiyuan Ma[a]

[a]Key Laboratory of Green Chemical Engineering and Technology of College of Heilongjiang Province, School of Materials Science and Chemical Engineering, Harbin University of Science and Technology, Harbin 150040, P. R. China

[b]Heilongjiang Electric Power Research Institute, State Grid, Harbin 150030, P. R. China

E-mail: wangxinming20@126.com; panghj116@163.com

Contents

Section 1 Additional Experimental Section

1. Chemicals and materials
2. Preparation of modified electrodes
3. Electrochemical measurements
4. Determination of NH_3
5. Determination of by-product nitrite
6. Determination of FE and NH_3 yield rate
7. The control experiments of the $^{15}N_2$ isotopic measurements to prove the nitrogen source

Section 2 Supplementary Figures and tables

Figure S1. TEM of Co-P_4Mo_6/GO

Figure S2. SEM of Ni-P_4Mo_6/GO

Figure S3. SEM of Co-P_4Mo_6/GO

Figure S4. XPS elemental spectra of Co-P_4Mo_6/GO

Figure S5. UV-vis absorption spectra of different NH_4Cl concentrations measured in 0.1 mol L^{-1} Na_2SO_4 electrolyte and corresponding standard curve of NH_4Cl

Figure S6. UV-vis absorption spectra of different NH_4Cl concentrations measured in 0.05 mol L^{-1} H_2SO_4 electrolyte and corresponding standard curve of NH_4Cl

Figure S7. UV-vis absorption spectra of different NO_2^- concentrations measured in 0.1 mol L^{-1} Na_2SO_4 electrolyte and corresponding standard curve of NO_2^-

Figure S8. UV-vis absorption spectra of different NO_2^- concentrations measured in 0.05 mol L^{-1} H_2SO_4electrolyte and corresponding standard curve of NO_2^-

Figure S9. Electrochemical tests and UV-vis absorption spectra of Ni-P_4Mo_6 / GO and Co-P_4Mo_6/GO under acidic conditions

Figure S10. Electrochemical tests and UV-vis absorption spectra of Ni-P_4Mo_6/GO and Co-P_4Mo_6/GO under neutral conditions

Figure S11. The LSV curves of Ni-P_4Mo_6/GO in different concentrations of NO_3^- electrolytes

Figure S12. UV-vis absorption spectra of NO_2^-

Figure S13. Bode plots of Ni-P_4Mo_6/GO, Co-P_4Mo_6/GO and GO

Figure S14. The electrochemical active area (ECSA) of Ni-P_4Mo_6/GO and Co-P_4Mo_6/GO

Figure S15. XPS spectra of the Ni-P_4Mo_6/GO catalyst after catalysis

Table S1. Crystal data and structure refinements for Ni-P_4Mo_6 and Co-P_4Mo_6

Table S2. Catalytic performance of Ni-P_4Mo_6/GO in different concentrations of nitrate electrolytes

Table S3. Comparison of electrochemical Performance of Ni-P_4Mo_6/GO with Reported Electrocatalysts

Section 3 References

Section 1 Additional Experimental Section:

1. Chemicals and materials

All chemicals are used directly without further purification. Nickel chloride hydrate ($NiCl_2·6H_2O$,99.9%), cobalt chloride hexahydrate($CoCl_2·6H_2O$,99.9%), ammonium paramolybdate tetrahydrate ($(NH_4)_6Mo_7O_{24}·24H_2O$,99.9%), ethanol ($CH_3CH_2OH$), anhydrous ethanol, sodium nitroferricyanide ($Na_2[Fe(CN)_5(NO)]·2H_2O$), acetone (C_3H_6O), polyethyleneimine (C_2H_5N), phosphoric acid (H_3PO_4,85%) were purchased from Tianjin Fu Yu Fine Chemical Co., Ltd. Sulfuric acid (H_2SO_4), salicylic acid ($C_7H_6O_3$), sodium nitrate ($NaNO_3$), sodium nitrite ($NaNO_2$), potassium bromide (KBr), p-aminobenzenesulfonic acid ($C_6H_7NO_3S$), isopropanol (C_3H_8O,99.5%) were purchased from Shanghai Macklin Company. 2-(4-(4-carboxyphenyl) phenyl) imidazo (4,5-f) (1,10) phenanthroline (HNCP) was purchased from Jinan Henghua Technology Co., Ltd. Academic Translation: Nafion and sodium citrate ($C_6H_5Na_3O_7$) were purchased from SIGMA-ALDRICH. Argon gas (Ar, high purity, 99.9999%) was purchased from Qinghua Gas Company. The carbon cloth (CC) was purchased from CeTech company. The sample was pretreated in HNO_3, and then ultrasonically treated several times in acetone, water and ethanol to remove surface impurities. $^{15}N_2$ isotope (99% N enrichment) was obtained from Shanghai Institute of Chemical Technology Co, Ltd. Deionized water was used in all experiments.

2. Preparation of modified electrodes

The carbon cloth (CC) was used as the electrode substrate, and the impurities were removed by acetone solution, anhydrous ethanol and deionized water in turn. CC was put into the reactor, and CC was completely immersed in concentrated nitric acid, and the reaction was carried out at 120 °C for 2 h. The treated carbon cloth was taken out, rinsed with deionized water to neutral pH, dried and cut into 1 cm×1 cm size for later use.

The 0.2 g sample material was fully ground with 0.2 g acetylene black. The ground sample (3 mg), 125 μL isopropanol, 10 μL Nafion solution and 365 μL H_2O were placed in a 10 mL centrifuge tube and mixed ultrasonically for 2 h. The working electrode was obtained by dropping 25 μL of mixed suspension on a 1 cm×1 cm carbon cloth and

standing for 10 h to dry naturally.

3. Electrochemical measurements

The electrochemical measurements were carried out on a CHI 760E electrochemical workstation in an H-type double electrolytic cell divided by Nafion 211 membrane. The catalyst/CC was used as the working electrode, the Ag/AgCl electrode was used as the reference electrode, and the platinum electrode was used as the counter electrode. All potential values were converted according to the Nernst equation (E vs. RHE) = E (vs. Ag/AgCl)+0.197+0.059×pH). Before the e-NO_3RR experiment, in order to ensure the accuracy of the experiment, it is necessary to purge the argon gas in the cathode chamber of the H-type electrode groove to avoid the influence of N_2 on the experimental results. For the e-NO_3RR experiment, the LSV curve test of the catalyst was carried out under two electrolyte conditions of 0.1 M $NaNO_3$+0.05 M H_2SO_4 (with NO_3^-) and 0.05 M H_2SO_4 (without NO_3^-) at room temperature and pressure, and the corresponding chronoamperometric (j−t) test was carried out in 0.1 M$NaNO_3$+0.1 M Na_2SO_4 electrolyte. In order to estimate the electrochemically active surface area (ESCA) of the catalyst, the double-layer capacitance (C_{dl}) was measured by cyclic voltammetry (CV) at a scan rate of 5-100 mV s^{-1} in the voltage range of −0.4 V vs. RHE to −0.5 V vs. RHE. Electrochemical impedance spectroscopy (EIS) measurements were carried out from 0.1 Hz to 1000 kHz with an amplitude of 10 mV at the open-circuit voltage.

4. Determination of NH_3

Ammonia production was analyzed by indophenol blue spectrophotometry, and standard ammonia solutions with concentrations of 1, 3, 6, 9 and 12 μg L^{-1} were prepared by dissolving ammonium chloride (NH_4Cl) in the corresponding electrolyte. Each 2.0 mL of the corresponding concentration of ammonia standard solution was added to 2.0 mL of salicylic acid and sodium citrate dihydrate in 5% 1M NaOH solution, respectively, and then 1.0 mL of 0.05 M sodium hypochlorite (NaClO) solution and 1% sodium nitroferricyanide solution were mixed evenly. The solution was placed in the dark for color development for 2 h. After the color development was completed, the absorbance (characteristic absorption peak 655 nm) was measured by ultraviolet

spectrophotometer to obtain the absorbance curve and draw the standard curve. In neutral electrolyte and acidic electrolyte, the linear equation obtained by ammonia standard curve fittings are Y=0.227X+0.0904 (neutral electrolyte) (Figure S5) and Y=0.223X−0.00418 (acidic electrolyte) (Figure S6).

5. Determination of by-product nitrite

In order to further explain the performance of the catalyst, the nitrite yield was analyzed by hydrochloric acid naphthalene ethylenediamine spectrophotometry. Similar to the preparation of ammonia standard solution, 0.5, 1, 1.5, 2.5 and 3.5 μg L^{-1} concentrations of nitrite standard solution were prepared. The color reagent and deionized water were mixed in a ratio of 4:1 to obtain a standard color solution. The 1 mL standard solution was added with 9 mL standard color solution, shaken well and allowed to stand in the dark for 15 min. The test was performed using an ultraviolet spectrophotometer (characteristic absorption peak 540 nm). The absorbance curve was obtained and the standard curve was drawn. In neutral electrolyte, the linear relationship is Y=0.089X+0.0159 (Figure S7). In acidic electrolyte, the linear relationship is Y=0.0435X−0.0015 (Figure S8).

6. Determination of FE and NH_3 yield rate

The performance of the catalyst was evaluated by indicators such as ammonia production and Faraday efficiency. The Faraday efficiency in the e-NO_3RR process was calculated by the following equation:

$$\text{Faraday efficiency } (FE_{NH_3}) = (8F \times C(NH_3) \times V)/(17Q)$$

The amount of ammonia produced in the e-NO_3RR process passes the following equation:

$$NH_3 \text{ yield} = (C(NH_3) \times V)/(m_{cat.} \times t)$$

The by-products in the e-NO_3RR process are detected, in which the nitrite production and Faraday efficiency are determined by the following equation:

$$FE_{NO_2^-} = 2F \times C(NO_2^-) \times V/(46Q)$$

$$NO_2^- \text{ yield} = C(NH_3) \times V/(t \times m_{cat.})$$

Where F is Faraday constant, Q is the amount of charge for several hours of

electrolysis, V is Volume of electrolyte in cathode chamber, $C(NH_3)$ is ammonia concentration in solution, $C(NO_2^-)$ is nitrite concentration in solution, $m_{cat.}$ is catalyst loading.

7. The control experiments of the $^{15}N_2$ isotopic measurements to prove the nitrogen source

The ^{15}N isotopic measurements were performed using the $^{15}N_2$ isotope with the ^{15}N (enrichment of ＞99%) to clarify the nitrogen origination of ammonia. Before the electrochemical reduction procedure, the electrolyte (pH 3.5, 1.0 mol L^{-1} of K^+) was purged with high-purity Ar to remove the ^{14}N from solution and thenwas pre-saturated with $^{15}N_2$ for 30 min with a flow rate of 10 mL min^{-1} (a low-velocity gas flow was adopted due to the limited supply and expense of $^{15}N_2$). The cathode electrolyte is 0.5 M $Na^{15}NO_3$ ($^{15}N \geqslant 99\%$ atom) + 0.1M Na_2SO_4. After 1 h electrolysis at –1.1 V vs. RHE, the 10 mL of the electrolyte was taken out and used for ^1H NMR detection. (^1H NMR, Bruker Avance NEO 600).

Section 2 Supplementary Figures and Tables:

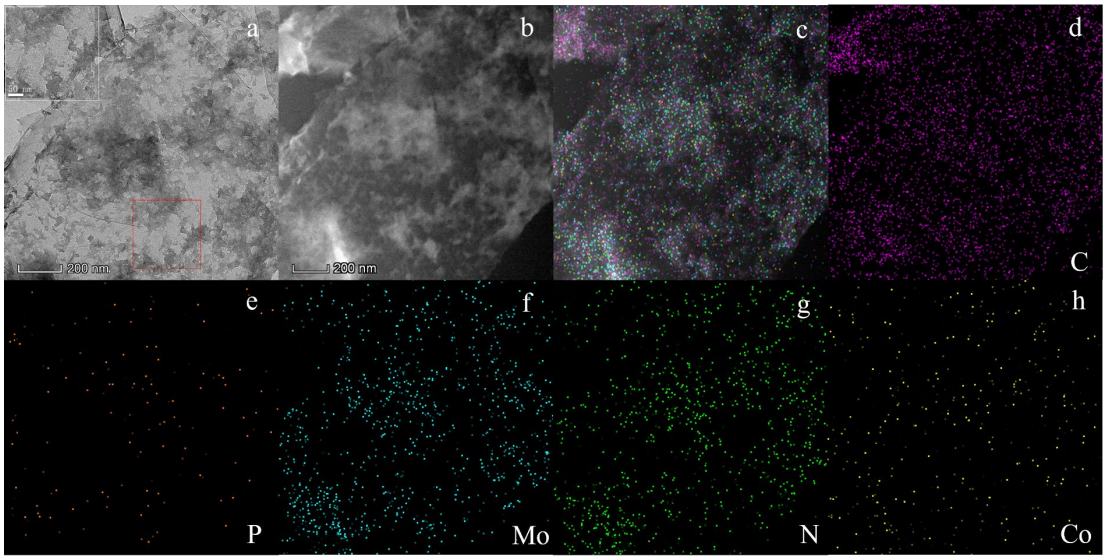

Figure S1. (a−b) TEM of Co-P_4Mo_6/GO. (c−f) Element mapping of images of Co-P_4Mo_6/GO.

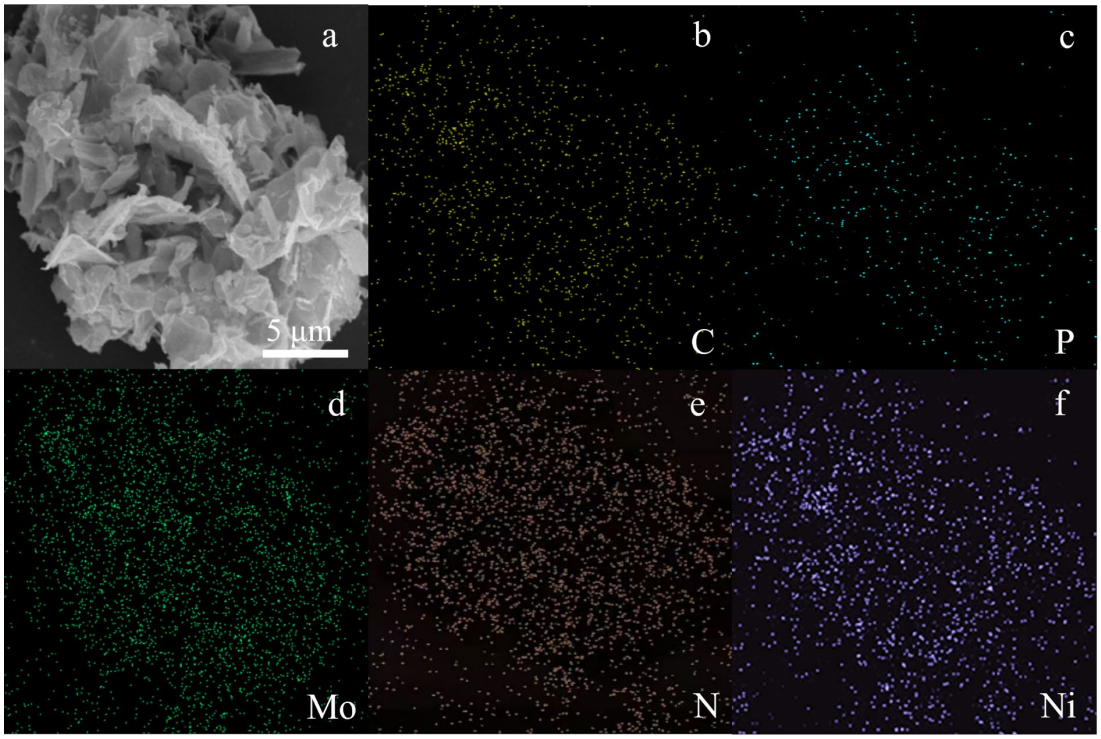

Figure S2. (a) SEM of Ni-P_4Mo_6/GO. (b–f) Element mapping of images of Ni-P_4Mo_6/GO.

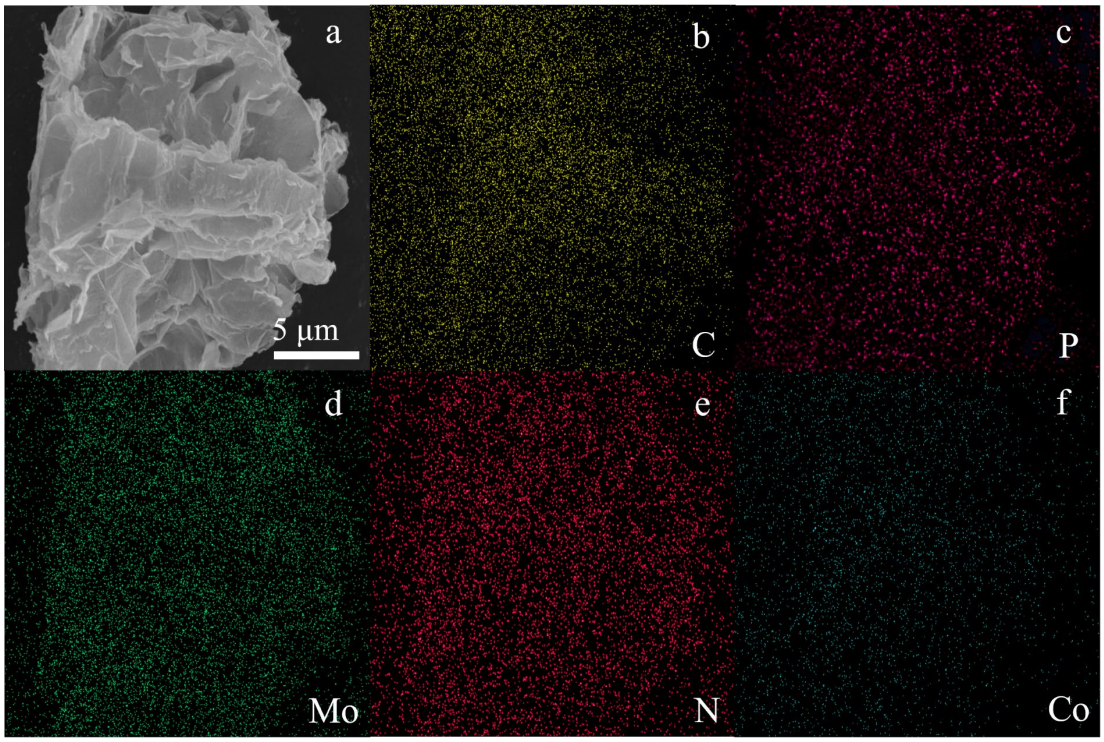

Figure S3. (a) SEM of Co-P_4Mo_6/GO. (b–f) Element mapping of images of Co-P_4Mo_6/GO.

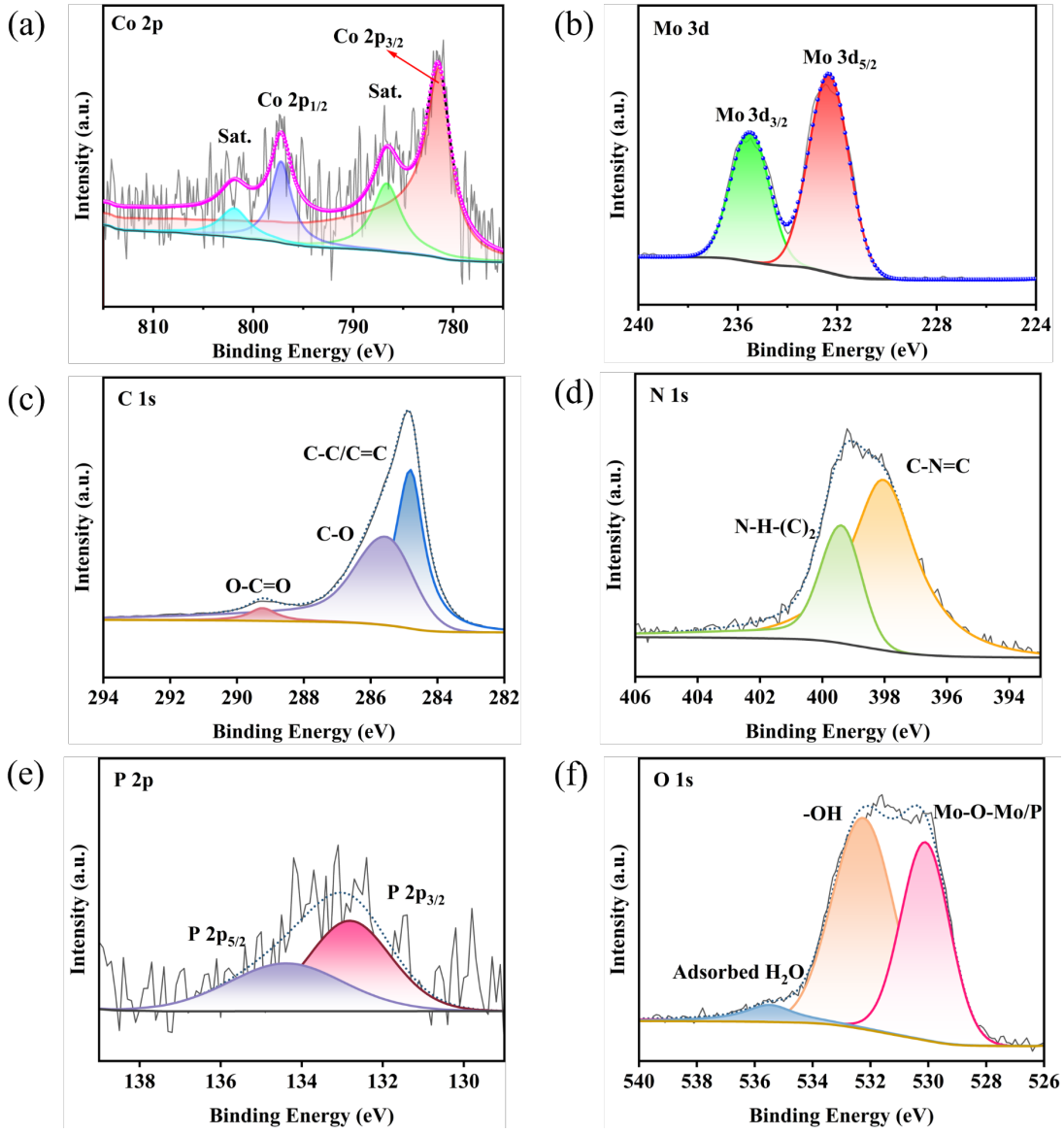

Figure S4. XPS elemental spectra of (a) Co 2p (b) Mo 3d (c) C 1s (d) O 1s (e) N 1s (f) P 2p in Co-P_4Mo_6/GO.

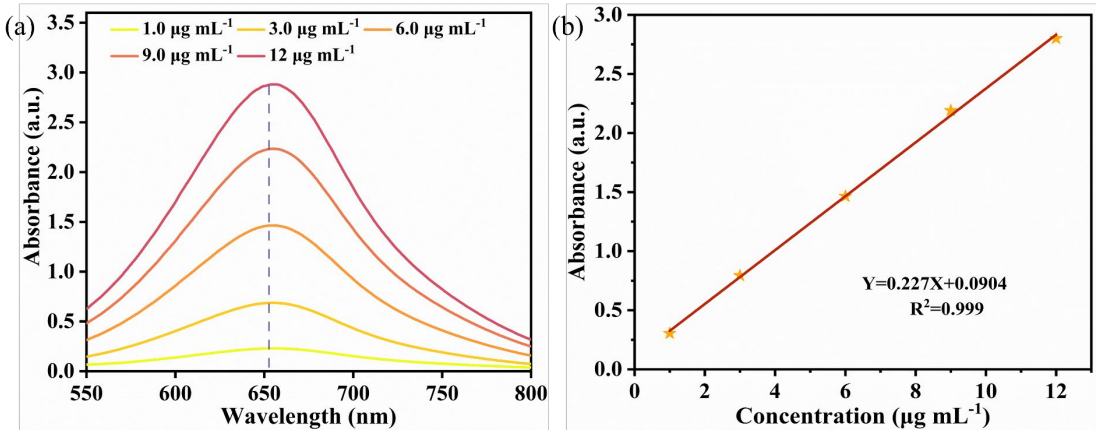

Figure S5. (a) UV-vis absorption spectra of different NH_4Cl concentrations measured in 0.1 mol L^{-1} Na_2SO_4 electrolyte. (b) Corresponding standard curve of NH_4Cl.

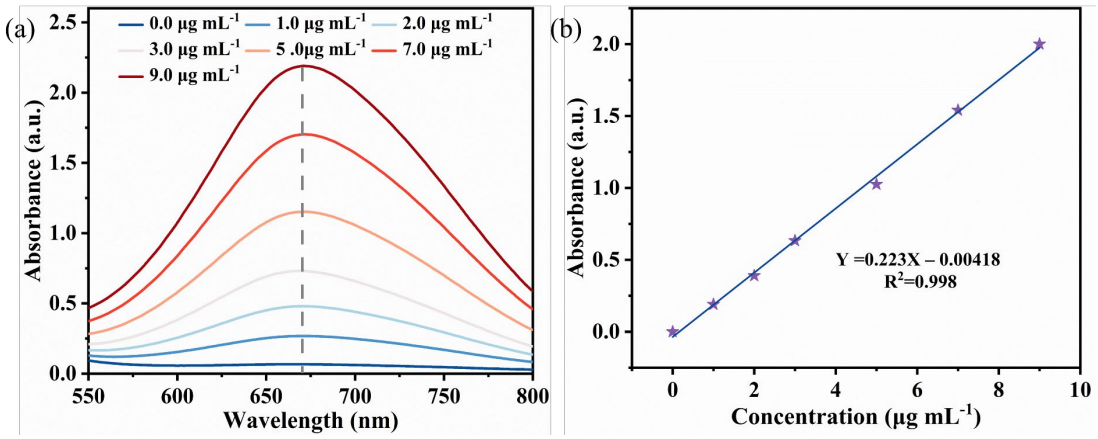

Figure S6. (a) UV-vis absorption spectra of different NH_4Cl concentrations measured in 0.05 mol L^{-1} H_2SO_4 electrolyte. (b) Corresponding standard curve of NH_4Cl.

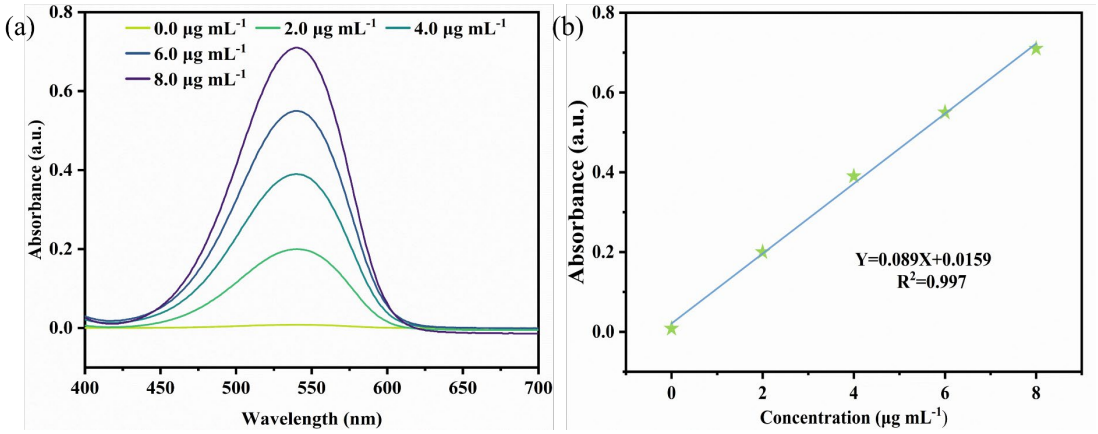

Figure S7. (a) UV-vis absorption spectra of different NO_2^- concentrations measured in 0.1 mol L^{-1} Na_2SO_4 electrolyte. (b) Corresponding standard curve of NO_2^-

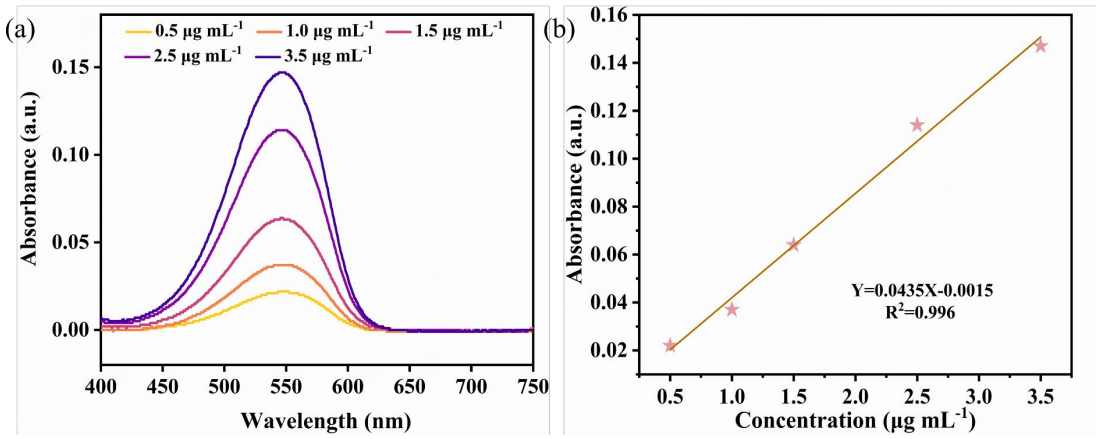

Figure S8. (a) UV-vis absorption spectra of different NO_2^- concentrations measured in 0.05 mol L^{-1} H_2SO_4electrolyte. (b) Corresponding standard curve of NO_2^-

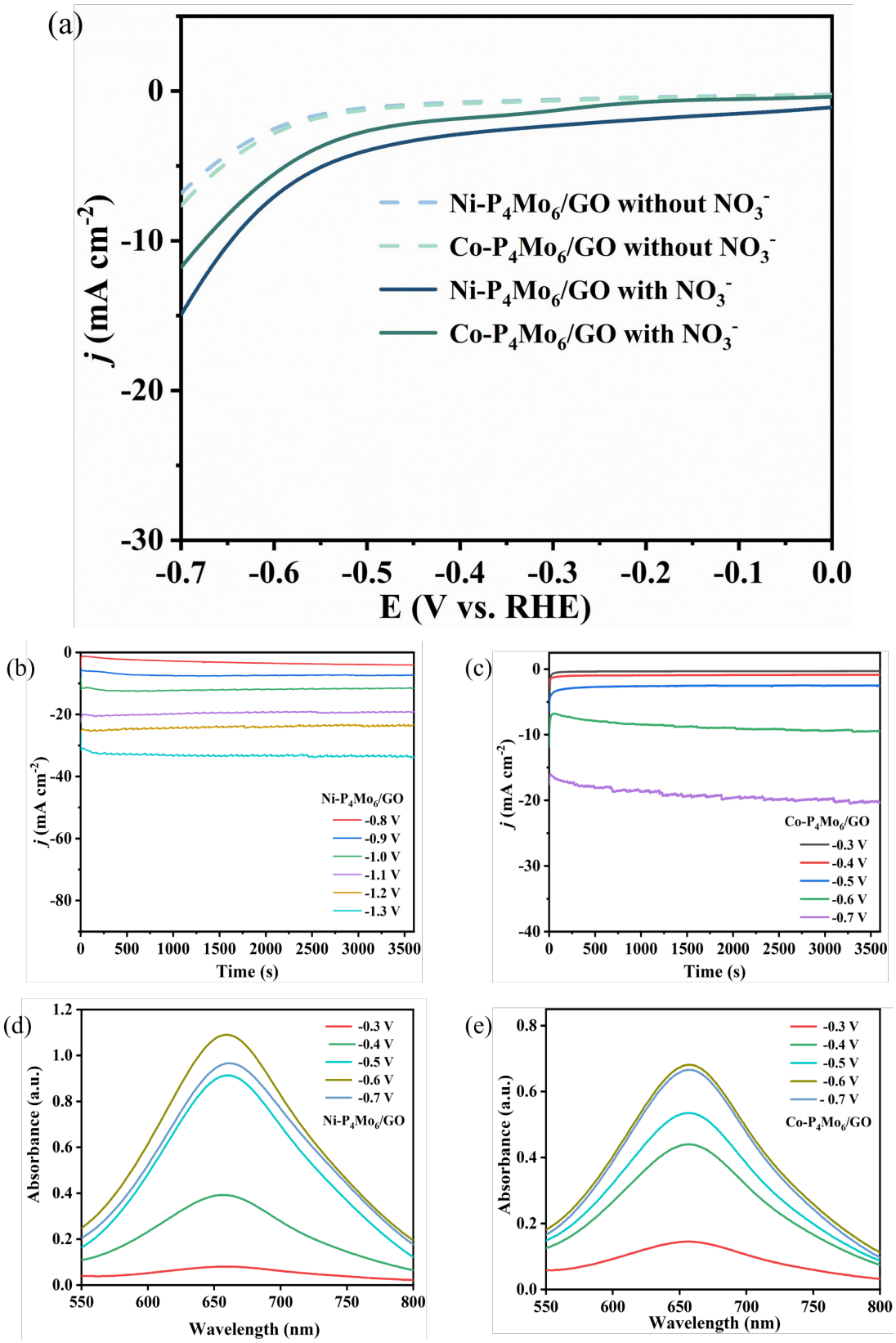

Figure S9. (a) LSV curves of Ni-P_4Mo_6/GO and Co-P_4Mo_6/GO. (b–c) Corresponding chronoamperometric (j–t) curves at various potentials of Ni-P_4Mo_6/GO and Co-P_4Mo_6/GO. (d-e) UV-vis absorption spectra of Ni-P_4Mo_6/GO and Co-P_4Mo_6/GO.

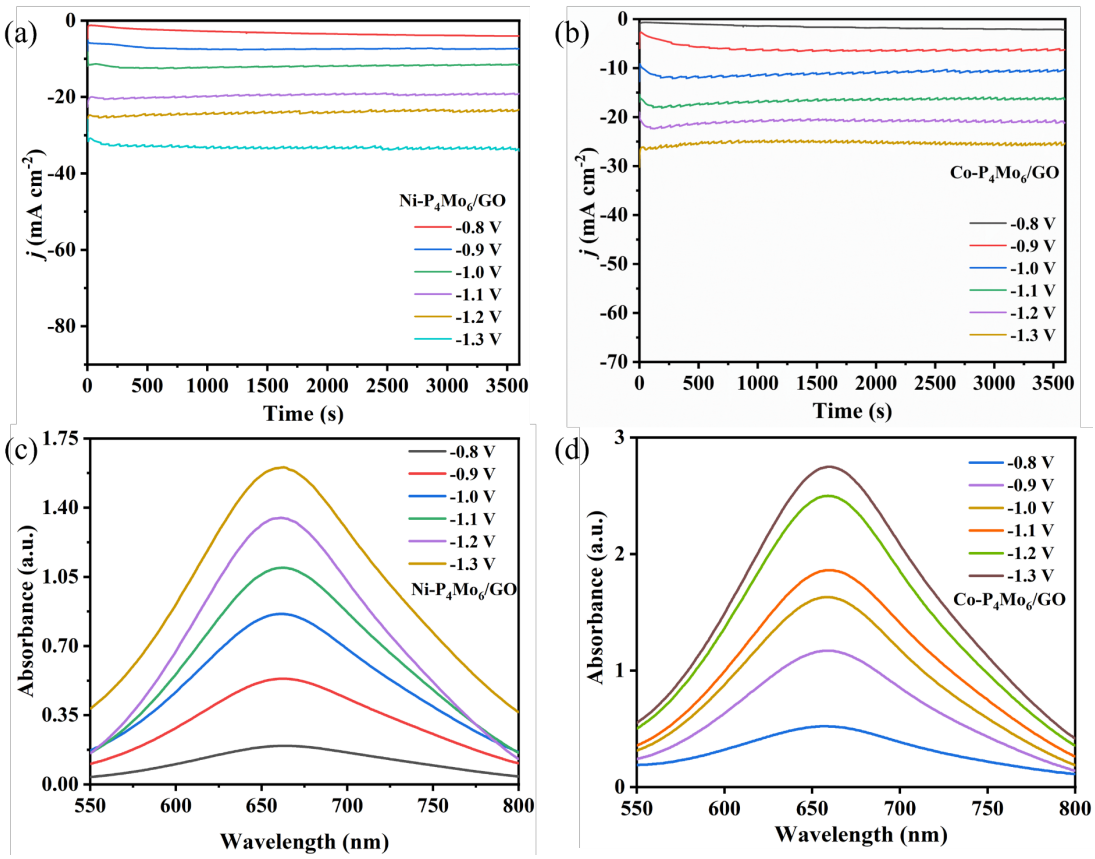

Figure S10. (a–b) Corresponding chronoamperometric (j–t) curves at various potentials. (c–d) UV-vis absorption spectra.

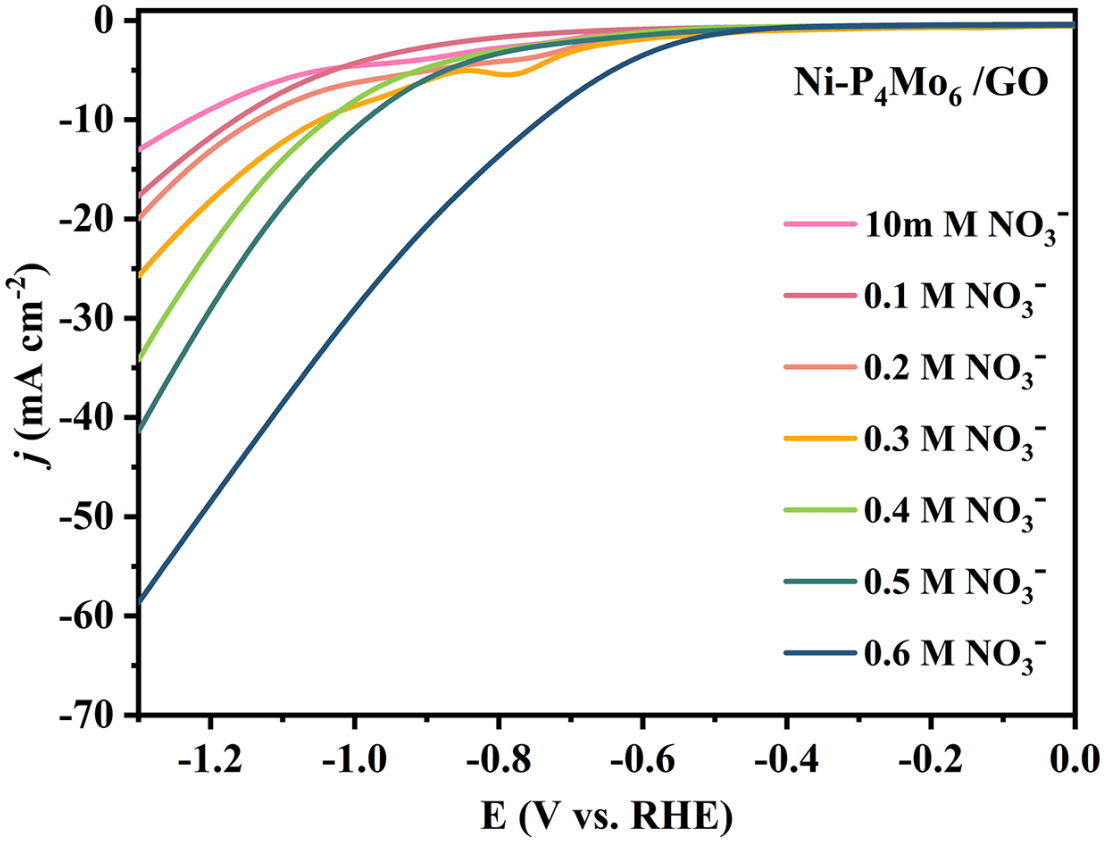

Figure S11. The LSV curves of Ni-P_4Mo_6/GO in different concentrations of NO_3^- electrolytes.

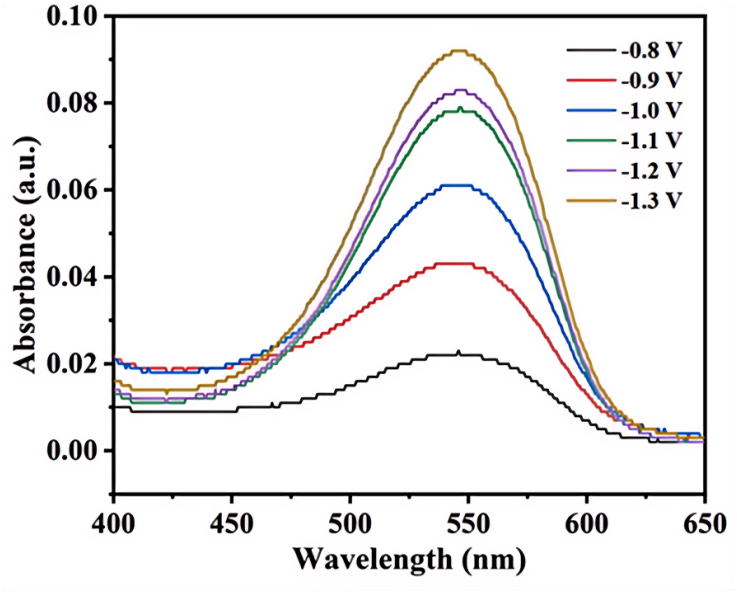

Figure S12. UV-vis absorption spectra of NO_2^-

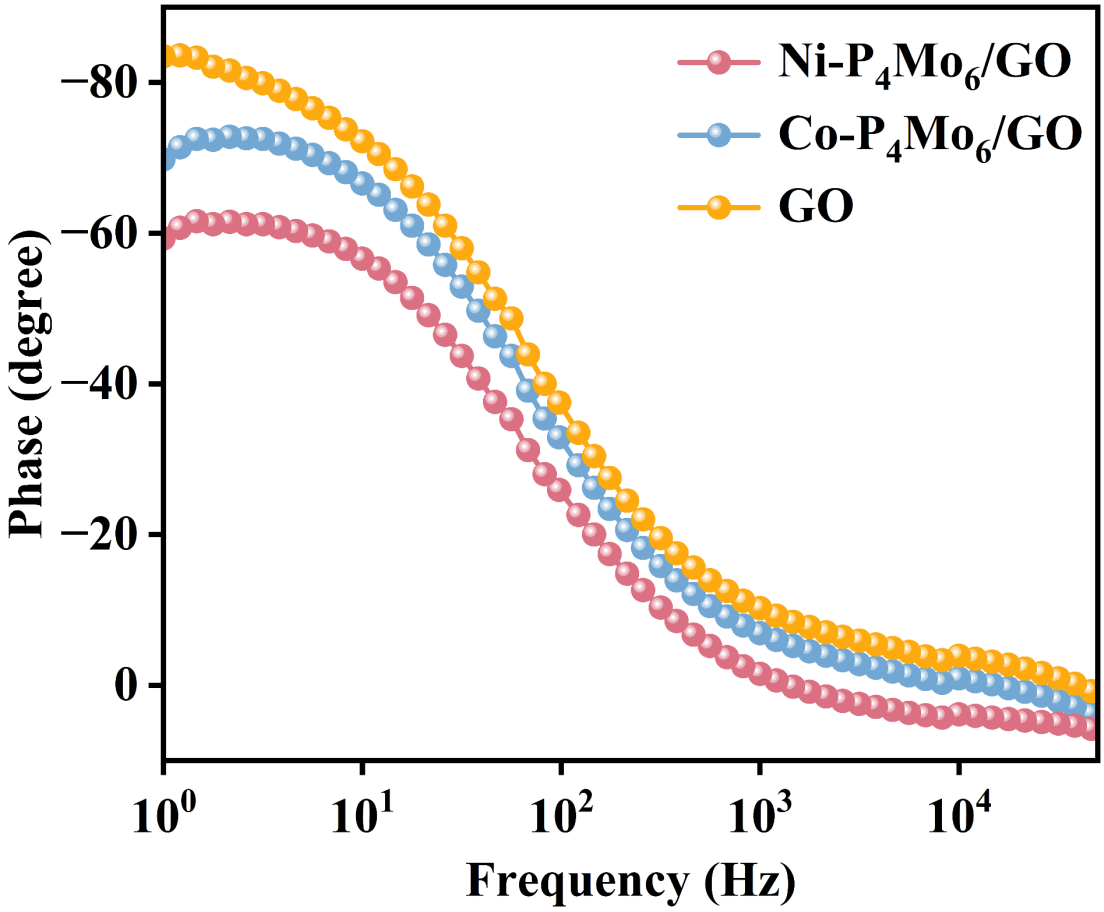

Figure S13. Bode plots of Ni-P_4Mo_6/GO, Co-P_4Mo_6/GO and GO.

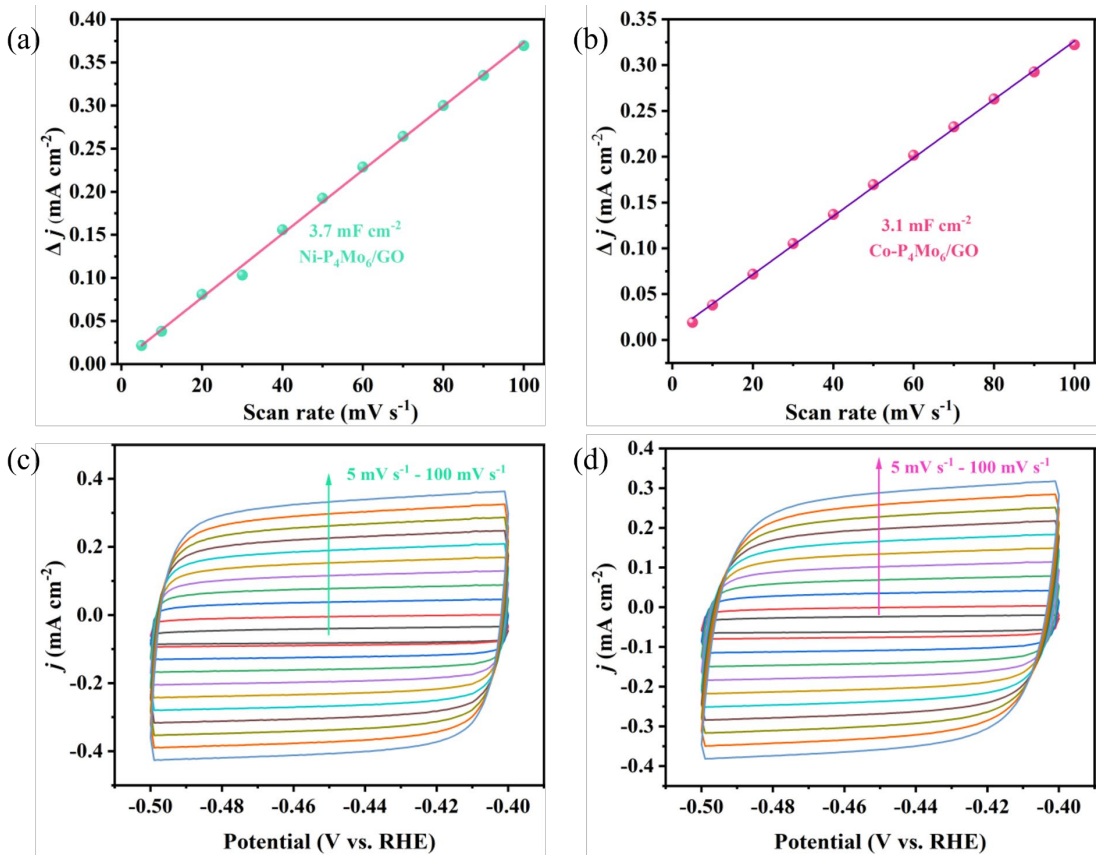

Figure S14. A series of CV tests were carried out in the voltage range of–0.4 V vs. RHE to –0.5 V vs. RHE at a scan rate of 5~100 mV s^{-1}. The electric double layer capacitance (C_{dl}) was calculated and its electrochemical active area (ECSA) was obtained: (a–b) the current density-scan rate plots. (c–d) The cyclic voltammetry curves.

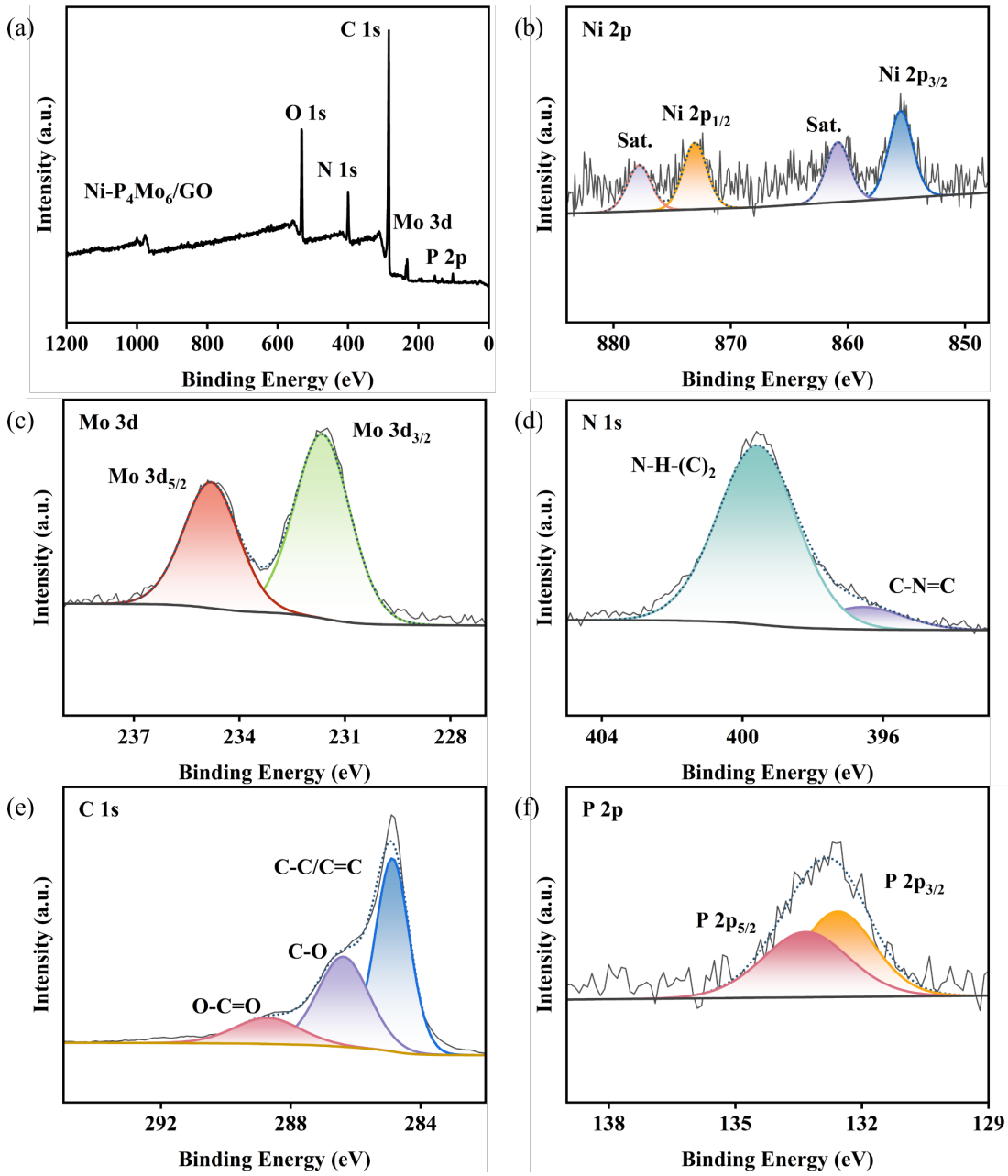

Figure S15 Structural analysis of Ni-P4Mo6/GO catalyst after reaction: (a) XPS survey spectra of Ni-P4Mo6/GO. (b) Ni 2p (c) Mo 3d (d) N 1s (e) C 1s (f) P 2p.

Table S1. Crystal data and structure refinements for Ni-P_4Mo_6 and Co-P_4Mo_6

	Ni-P_4Mo_6	Co-P_4Mo_6
formula	$C_{40}H_{44}Mo_{12}N_8Ni_3O_{74}P_8$	$C_{40}H_{44}Mo_{12}N_8Co_3O_{74}P_8$
Formula weight	3396.00	3396.66
Crystal system	Triclinic	Triclinic
space group	Pī	Pī
a (Å)	13.238(3)	13.344(11)
b (Å)	14.079(4)	14.170(12)
c (Å)	14.549(4)	14.594(12)
α (°)	71.048(3)	71.113(10)
β (°)	80.242(4)	80.013(10)
γ (°)	75.906(4)	75.607(10)
V ($Å^3$)	2475.4(11)	2515.9(4)
Z	1	1
D_c (g cm^{-3})	2.278	2.242
μ (mm^{-1})	2.264	2.161
F(000)	1640.0	1637.0
R_1[a][I > 2σ(I)]	0.0256	0.0251
wR_2[b](all data)	0.0753	0.0722
GOF on F^2	1.043	1.056
CCDC	2426711	2426712

[a]$R_1 = \sum||F_o| - |F_c|| / |F_o|$. [b]$wR_2 = \{\sum[w(F_o^2-F_c^2)^2] / \sum[w(F_o^2)^2]\}^{1/2}$

Table S2. Catalytic performance of Ni-P_4Mo_6/GO in different concentrations of nitrate electrolytes

Nitrate concentration (M)	NH_3 Yield (mg h^{-1} $mg^{-1}_{cat.}$)	Corresponding voltage (V vs. RHE)	FE (%)	Corresponding voltage (V vs. RHE)
0.01	1.05	–1.2	45.2	–0.9
0.1	4.52	–1.3	73.2	–0.9
0.2	4.45	–1.3	75.5	–1.1
0.3	8.51	–1.3	82.5	–0.9
0.4	8.74	–1.3	83.7	–1.0
0.5	11.59	–1.3	88.45	–1.1
0.6	10.42	–1.3	82.1	–1.0

Table S3. Comparison of electrochemical Performance of Ni-P_4Mo_6/GO with Reported Electrocatalysts

Catalysts	NH_3 Yield	FE(%)	Applied Potential vs RHE	Ref
Ni-P_4Mo_6/GO	11.6 mg h^{-1} $mg^{-1}_{cat.}$	88.4	–1.3	This work
Co-P_4Mo_6/GO	11.1 mg h^{-1} $mg^{-1}_{cat.}$	78.5	–1.1	This work
Cu-BTC-Cu	4.00 mg h^{-1} $cm^{-2}_{cat.}$	83.8	–1.0	[1]
$Fe(TCNQ)_2$	11. 35 mg h^{-1} cm^{-2}	85.2	–1.1	[2]
Pd(111)	2.74 mmol h^{-1} mg^{-1}	79.9	–0.7	[3]
PP-Co/CP	1.1 mmol h^{-1} $mg^{-1}_{cat.}$	90.1	–0.7	[4]
IrNTs	921 μg h^{-1} $mg^{-1}_{cat.}$	84.7	–0.06	[5]
Pd/TiO_2	1.12 mg cm^{-2} h^{-1}	92.1	–0.8	[6]
$Cu/Pd/CuO_x$	1510.33 μg $h^{-1}mg^{-1}$	84.04	–1.3	[7]
Co_3O_4/Co	4.43 mg h^{-1} cm^{-2}	88.7	–0.8	[8]
$La_2Cu_{0.8}Co_{0.24}$	0.07mmol h^{-1} mg^{-1}	75.3	–0.68	[9]
Cu@C	469.5μg h^{-1} cm^{-2}	72.0	–0.9	[10]
Co/NC-800	1352.5μg $h^{-1}mg^{-1}$	81.2	–1.7	[11]
CoNi-Vp-x	0.098 mmol h^{-1} cm^{-2}	84.27	–1.7	[12]

Section 3 References

References

[1] Wang, Y.; Cao, Y.; Hai, Y.; Wang, X.; Su, S.; Ding, W.; Liu, Z.; Li, X.; Luo, M. Metal–organic framework-derived Cu nanoparticle binder-free monolithic electrodes with multiple support structures for electrocatalytic nitrate reduction to ammonia. *Dalton Transactions* **2023**, *52* (32), 11213-11221.

[2] Mukherjee, N.; Adalder, A.; Barman, N.; Thapa, R.; Urkude, R.; Ghosh, B.; Ghorai, U. K. $Fe(TCNQ)_2$ nanorod arrays: an efficient electrocatalyst for electrochemical ammonia synthesis via the nitrate reduction reaction. *Journal of Materials Chemistry A* **2024**, *12* (6), 3352-3361.

[3] Han, Y.; Zhang, X.; Cai, W.; Zhao, H.; Zhang, Y.; Sun, Y.; Hu, Z.; Li, S.; Lai, J.; Wang, L. Facet-controlled palladium nanocrystalline for enhanced nitrate reduction towards ammonia. *Journal of Colloid and Interface Science* **2021**, *600*, 620-628.

[4] Zhao, J.-W.; Li, Y.-Z.; Chen, L.-J.; Yang, G.-Y. Research progress on polyoxometalate-based transition-metal–rare-earth heterometallic derived materials: synthetic strategies, structural overview and functional applications. *Chemical Communications* **2016**, *52* (24), 4418-4445.

[5] Zhu, J.-Y.; Xue, Q.; Xue, Y.-Y.; Ding, Y.; Li, F.-M.; Jin, P.; Chen, P.; Chen, Y. Iridium Nanotubes as Bifunctional Electrocatalysts for Oxygen Evolution and Nitrate Reduction Reactions. *ACS Applied Materials & Interfaces* **2020**, *12* (12), 14064-14070.

[6] Guo, Y.; Zhang, R.; Zhang, S.; Zhao, Y.; Yang, Q.; Huang, Z.; Dong, B.; Zhi, C. Pd doping-weakened intermediate adsorption to promote electrocatalytic nitrate reduction on TiO_2 nanoarrays for ammonia production and energy supply with zinc–nitrate batteries. *Energy & Environmental Science* **2021**, *14* (7), 3938-3944.

[7] Ren, T.; Yu, Z.; Yu, H.; Deng, K.; Wang, Z.; Li, X.; Wang, H.; Wang, L.; Xu, Y. Interfacial polarization in metal-organic framework reconstructed Cu/Pd/CuOx multi-phase heterostructures for electrocatalytic nitrate reduction to ammonia. *Applied Catalysis B: Environmental* **2022**, *318*, 121805.

[8] Fan, X.; Liang, J.; Zhang, L.; Zhao, D.; Yue, L.; Luo, Y.; Liu, Q.; Xie, L.; Li, N.; Tang, B.; et al. Enhanced electrocatalytic nitrate reduction to ammonia using plasma-induced oxygen vacancies in $CoTiO_{3-x}$ nanofiber. *Carbon Neutralization* **2022**, *1* (1), 6-13.

[9] Gong, Z.; Zhong, W.; He, Z.; Jia, C.; Zhou, D.; Zhang, N.; Kang, X.; Chen, Y. Improving electrochemical nitrate reduction activity of layered perovskite oxide La_2CuO_4 via B-site doping. *Catalysis Today* **2022**, *402*, 259-265.

[10] Song, Z.; Liu, Y.; Zhong, Y.; Guo, Q.; Zeng, J.; Geng, Z. Efficient Electroreduction of Nitrate into Ammonia at Ultralow Concentrations Via an Enrichment Effect. *Advanced Materials* **2022**, *34* (36), 04306.

[11] Liu, H.; Qin, J.; Mu, J.; Liu, B. In situ interface engineered Co/NC derived from ZIF-67 as an efficient electrocatalyst for nitrate reduction to ammonia. *Journal of Colloid and Interface Science* **2023**, *636*, 134-140.

[12] Gao, Y.; Wang, K.; Xu, C.; Fang, H.; Yu, H.; Zhang, H.; Li, S.; Li, C.; Huang, F. Enhanced electrocatalytic nitrate reduction through phosphorus-vacancy-mediated kinetics in heterogeneous bimetallic phosphide hollow nanotube array. *Applied Catalysis B: Environmental* **2023**, *330*, 122627.